Available online at www.sciencedirect.com
SCIENCE DIRECT®
Journal of Computational Physics 201 (2004) 511–530
JOURNAL OF COMPUTATIONAL PHYSICS
www.elsevier.com/locate/jcp

Numerical simulations of the quantized vortices on a thin superconducting hollow sphere ☆

Qiang Du [a,*], Lili Ju [b]

[a] Department of Mathematics, Pennsylvania State University, 218 McAllister Bldg, University Park, PA 16802, USA
[b] Institute for Mathematics and its Applications, University of Minnesota, Minneapolis, MN 55455, USA

Received 23 September 2003; received in revised form 27 May 2004; accepted 11 June 2004
Available online 24 July 2004

Abstract

In this paper, we investigate the vortex nucleation on a thin superconducting hollow sphere. The problem is studied using a simplified system of Ginzburg–Landau equations. We present numerical algorithms which preserve the discrete gauge invariance for both time dependent and time independent simulations. The spatial discretization is based on a spherical centroidal Voronoi tessellation which offers a very effective high resolution mesh on the sphere for the order parameter as well as other physically interesting variables such as the super-current and the induced magnetic field. Various vortex configurations and energy diagrams are computed. Dynamic responses of the vortices to the applied current are also simulated.

Keywords: Quantized vortices; Ginzburg–Landau model of superconductivity; Finite volume methods; Spherical centroidal Voronoi tessellations

1. Introduction

The quantized vortex phenomena are well-known signatures of superfluidity that appear in superfluid helium, superconductors and Bose–Einstein condensates. The nucleation, motion and pinning of vortices in superconductors play important roles in the theoretical studies and the practical applications

☆ This work is supported in part by NSF-DMS 0196522 and NSF-ITR 0205232.
* Corresponding author. Tel.: +1-814-865-3674; fax: +1-814-865-3735.
E-mail addresses: qdu@math.psu.edu, qud2@psu.edu (Q. Du), ju@ima.umn.edu (L. Ju).

0021-9991/$ - see front matter © 2004 Elsevier Inc. All rights reserved.
doi:10.1016/j.jcp.2004.06.009

of superconductivity. It has become even more clear in recent years that the geometry of the superconducting sample affects greatly the vortex nucleation patterns, see for example, [26,32,35,36]. In this paper, we consider a thin spherical superconducting shell and study the vortex patterns for this particular geometry nucleated by an applied magnetic field. Existing studies on superconducting samples with spherical geometry, ranging from superconducting balls to hollow spheres [8,11,41,42], have not provided a systematic description of the vortex nucleation phenomena. Due to the use of superconducting hollow spheres in the technological applications of superconductivity, for instance, in the superconducting gravimeters [34], the Gravity Probe B gyroscopes [30], and the latest development in superconducting nano-clusters [37,38], it is of both theoretical and practical interests to study the vortex structures related to the spherical geometries.

Quantized vortices in superconductors have often been modeled by the phenomenological model of Ginzburg and Landau [19,39]. Below the critical temperature, quantized vortices can be nucleated in a type-II superconductor when it is subject to an applied magnetic field above certain critical strength. The study of Abrikosov on the vortex lattices based on the Ginzburg–Landau (G–L) model was a Nobel prize winning work that has become the highlight of the impact of the G–L model on the study of superconductivity and quantum superfluidity. In recent years, the mathematical analysis, numerical approximations and large scale computations based on the G–L type models have also been made [1–3,7,14,19,20,23–25,27,28,31]. For a thin structure, a reduction of the full three dimensional G–L model can be made which leads to a simplified model that retains the basic features of the vortex state [5]. Similar to the case of a thin film [2,4,6], we hereby focus on solving the simplified equation using high quality spherical grids, the spherical centroidal Voronoi tessellations [18] (SCVT). By generalizing the finite volume approximation for the convection diffusion equations on such grids [18,21], a gauge invariant approximation of the reduced steady state G–L model has been presented in [22]. Theoretical analysis and preliminary numerical studies have also been made there. Coupled with the recently developed SCVT as the underlying grid, the gauge invariant approximation provides a higher order resolution of the physical variables, including the density of the superconducting carriers, super-current and the induced magnetic field, than the conventional spherical Voronoi–Delaunay grids. To certain extent, the nonlinear G–L equations provides an ideal testing bed for the SCVT grid which is likely to find many applications in the numerical solution of other nonlinear problems defined on the sphere.

In this paper, we carry out much more detailed computational studies concerning the various vortex structures appearing in the nucleation process. We also extend the gauge invariant approximations to the time dependent models by utilizing a time integration factor technique. A novel and somewhat surprising property of our algorithms is the fact that, due to the gauge invariant approximation, a variational principle can be established for the time dependent simulation even when there is an applied current, thus allowing an efficient and unified implementation of the time dependent marching algorithm and leading to an effective time step control strategy. Standard time marching schemes, on the other hand, only obey such a variational principle in the absence of the applied current. Based on the numerical simulations given here, we are able to make some physically interesting observations on various issues such as the energy barriers between different vortex states, the hysteresis phenomena, the change of energy due to vortex annihilation and the periodic behavior of the current driven vortex motion. It is interesting to note that some of the simulation results are attributed to the topology/geometry of the thin spherical structure considered in this paper, further justifying the study of the G–L model for superconductors having different geometrical and topological features.

The paper is organized as follows. We first recall the basic G–L model and its time dependent version in Section 2. Then, a gauge invariant discretization based on the SCVT and the time integration factor are discussed in Section 3. In Section 4, the results of numerical simulations are presented. Final conclusions are given in Section 5.

2. The Ginzburg–Landau model for superconductivity

In a suitably non-dimensionalized form, the primary variables used in the G–L model [12,19,39] are the complex scalar-valued *order parameter* ψ, the real vector-valued *magnetic potential* $\mathbf{A}$, and the real scalar-valued *electric potential* Φ.

When the region Ω occupied by the superconducting sample forms a thin structure, a reduction of the original G–L models is possible [2,4]. For example, in the case of a thin spherical shell with constant thickness $\delta \ll 1$, the solution of the original three dimensional G–L models can be approximated, to the leading order of δ, by $(\psi,\mathbf{A}_0)$, where the function ψ is defined on the sphere surface $\mathbb{S}^2 = \{\mathbf{x} \mid \|\mathbf{x}\| = r > 0\}$ in the same spirits of the studies made for a thin film [5,10,22].

Given a constant applied magnetic field $\vec{H} = H\vec{z}$ in the z-direction, after a re-scaling, the reduced model equation satisfied by ψ can be formulated as

$$\frac{\partial \psi}{\partial t} + \mathrm{i}\Phi_0\psi - (\nabla_s - \mathrm{i}\mathbf{A}_{0s})^2\psi + \frac{1}{\epsilon^2}\psi(|\psi|^2 - 1) = 0, \quad \text{on } \mathbb{S}^2 \times (0,T), \tag{1}$$

with an initial condition $\psi(\mathbf{x},0) = \psi_0(\mathbf{x})$ on $\mathbb{S}^2$. Here, ∇_s is the surface tangential gradient [29] given by $\nabla_s = \nabla - (\nabla \cdot \vec{\mathbf{n}}_x)\vec{\mathbf{n}}_x$ where ∇ is the standard gradient operator and $\vec{\mathbf{n}}_x = \mathbf{x}/\|\mathbf{x}\|$ is the outer normal of $\mathbb{S}^2$ at $\mathbf{x}$. Φ_0 is a prescribed reduced scalar electric potential such that $\nabla\Phi_0$ represents an applied electric current (voltage) [16]. $\mathbf{A}_0 = \mathbf{A}_0(\mathbf{x}) = \frac{H}{2}(y,-x,0)^{\mathrm{T}}$ is a prescribed reduced vector magnetic potential and $\mathbf{A}_{0s} = \mathbf{A}_0 - (\mathbf{A}_0 \cdot \vec{\mathbf{n}}_x)\vec{\mathbf{n}}_x$ is the tangential projection of $\mathbf{A}_0$ on $\mathbb{S}^2$. The parameter ϵ can be interpreted as the effective coherence length for the thin spherical shell.

For the case of the zero applied current, the steady state equation is given by

$$-(\nabla_s - \mathrm{i}\mathbf{A}_{0s})^2\psi + \frac{1}{\epsilon^2}\psi(|\psi|^2 - 1) = 0, \quad \text{on } \mathbb{S}^2. \tag{2}$$

The steady state solutions of the above equation are the critical points of an effective free energy functional:

$$\mathscr{F}(\psi) = \int_{\mathbb{S}^2} \left(|(\nabla_s - \mathrm{i}\mathbf{A}_{0s})\psi|^2 + \frac{1}{2\epsilon^2}(1 - |\psi|^2)^2 \right) \mathrm{d}S, \tag{3}$$

which is a simplification of the original Gibbs free energy.

Both the functional $\mathscr{F}$ and the time dependent equations remain invariant under the gauge transformation:

$$(\psi, \mathbf{A}_{0s}, \Phi_0) \to \left(\psi \exp(\mathrm{i}\sigma), \mathbf{A}_{0s} + \nabla_s\sigma, \Phi_0 - \frac{\partial \sigma}{\partial t} \right) \tag{4}$$

for any smoothly defined real-valued scalar function $\sigma = \sigma(\mathbf{x},t)$.

Eq. (1) also can be written as

$$\frac{\partial \psi}{\partial t} + \mathrm{i}\Phi_0\psi = -\frac{1}{2}\frac{\partial \mathscr{F}}{\partial \psi}(\psi), \quad \text{on } \mathbb{S}^2 \times (0,T), \tag{5}$$

where $\partial\mathscr{F}/\partial\psi$ denotes the first variation of $\mathscr{F}$ with respect to ψ. For the case $\Phi_0 = 0$, it is often called a gradient flow [23]. Within the G–L framework, $|\psi|^2$ corresponds to the density of superconducting carriers – the so-called Cooper-pairs [19,39]; the state $|\psi| = 1$ corresponds to the Meissner superconducting state while the point at which $|\psi| = 0$ is called a vortex which is surrounded by a normal core and leads to the penetration of the magnetic flux.

One of our objective here is to compute the ground state of the energy, and calculate the various solution branches for (2). Accurate bifurcation diagrams can be drawn similar to the study made in [1]. We also investigate the nucleation process as well as the vortex motion due to an applied current by solving the time

dependent equation with both zero and nonzero electric potentials. Note that for very thin shells, the solution ψ gives very good approximations to the solution of the original G–L equations [4,5,16] so that the bifurcation diagrams and the vortex motion patterns computed from the reduced model give accurate descriptions of the vortex state in a three dimensional thin spherical shell.

3. Finite volume approximations

Given a set of distinct points $\{\mathbf{x}_j\}_{j=1}^n \subset \mathbb{S}^2$, a spherical Voronoi tessellation is defined as the union of the Voronoi regions (cells) $\{V_j\}_{j=1}^n$ of the form:

$$V_j = \{\mathbf{y} \in \mathbb{S}^2 \mid d(\mathbf{x}_j, \mathbf{y}) < d(\mathbf{x}_k, \mathbf{y}) \quad \text{for } k = 1, \ldots, n \text{ and } k \neq j\},$$

where $d(\mathbf{x}_k,\mathbf{y})$ denotes the geodesic distance from $\mathbf{x}_k$ to $\mathbf{y}$ on the sphere and $\{\mathbf{x}_j\}$ are called the *generators* (although the standard three dimensional Euclidean distance would give the same Voronoi regions [17]). The dual Delaunay triangulation to a Voronoi tessellation of $\mathbb{S}^2$ consists of spherical triangles with edges connecting neighboring generators. A SCVT [18,17,22] is a particular spherical Voronoi tessellation for which the generators coincide with the constrained mass centroids of the corresponding Voronoi cells with respect to some pre-defined density function $\rho = \rho(\mathbf{x})$ defined on $\mathbb{S}^2$ (see Fig. 1 for an illustration corresponding to a uniform constant density). For more discussion on the Centroidal Voronoi Tessellation (CVT), we refer to [15].

3.1. Discrete gauge invariant scheme

For the time dependent G–L equation, we take the gauge invariant backward Euler scheme for its discretization since such a method has unconditional stability (see [14] for some discussion in the planar case).

Let $\triangle t_k$ be the time step size at the kth step, $T_k = \sum_{m=1}^{k} \triangle t_m$, and $\Phi_{0j} = \Phi_0(\mathbf{x}_j)$. For a spherical Voronoi tessellation $\mathscr{W} = \{\mathbf{x}_j, V_j\}_{j=1}^n$ as the one depicted in Fig. 1, we define the unknowns as $\vec{\psi}_h^k = \vec{\psi}_h(T_k) = (\psi_1^k, \psi_2^k, \ldots, \psi_n^k)$ satisfying, for $j = 1,2,\ldots,n$, that

$$\frac{\psi_j^k - \exp(-\mathrm{i}\Phi_{0j}\triangle t_k)\psi_j^{k-1}}{\triangle t_k} = -\frac{1}{2}\frac{1}{m(V_j)}\frac{\partial \mathscr{F}^h}{\partial \psi_j^k}\left(\vec{\psi}_h^k\right), \tag{6}$$

where the discrete G–L functional $\mathscr{F}^h$ is given by [22]:

$$\mathscr{F}^h(\vec{\psi}_h) = \frac{1}{2\epsilon^2}\sum_{j=1}^{n}\left\{m(V_j)(1 - |\psi_j|^2)^2\right\} + \frac{1}{2}\sum_{j=1}^{n}\sum_{l\in\chi_j}\left\{\frac{m(\Gamma_{jl})}{\|\mathbf{x}_j - \mathbf{x}_l\|}\,|\,\psi_l \exp(-\mathrm{i}c_{jl}) - \psi_j|^2\right\}, \tag{7}$$

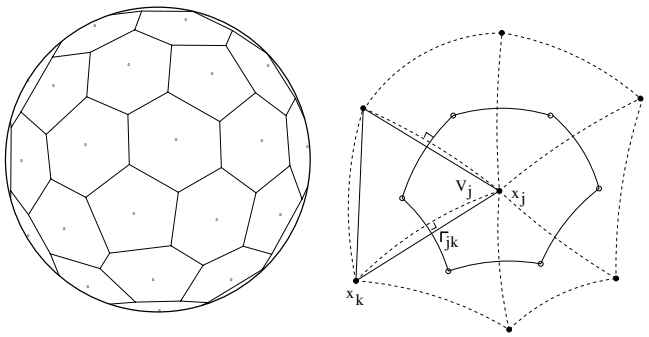

Fig. 1. Left: a SCVT; right: a single Voronoi region and its dual triangles.

with $\chi_j = \{k | m(\Gamma_{jk}) \neq 0\}$ being the index set of neighboring vertices, and

$$c_{jl} = \int_{\widetilde{\mathbf{x}_l \mathbf{x}_j}} \mathbf{A}_{0s}(\mathbf{x}) \cdot \vec{\mathbf{t}}_{jl}(\mathbf{x}) \mathrm{d}s,$$

and $\vec{\mathbf{t}}_{jl}(\mathbf{x})$ is used to denote the unit tangent field along the geodesic arc $\widetilde{\mathbf{x}_l \mathbf{x}_j}$, $m(\cdot)$ denotes either the spherical area or the geodesic arc length, and $\{\chi_j\}$ denotes the index set of all vertices adjacent to the vertex $\mathbf{x}_j$.

The time dependent discretization can be rewritten in more details as

$$\psi_j^k - \psi_j^{k-1} \exp(-\mathrm{i}\Phi_{0j} \triangle t_k) - \frac{\triangle t_k}{m(V_j)} \sum_{l \in \chi_j} m(\Gamma_{jl}) \frac{\psi_j^k \exp(-\mathrm{i}c_{jl}) - \psi_j^k}{\|\mathbf{x}_j - \mathbf{x}_l\|} + \frac{\triangle t_k}{\epsilon^2} \psi_j^k (|\psi_j^k|^2 - 1) = 0. \tag{8}$$

Both the time dependent numerical scheme and the discrete free energy functional preserve the discrete gauge invariance [14]. Moreover, it is easy to check that at each time step, the solution $\vec{\psi}_h^k$ is a critical point of the functional

$$\mathscr{K}^h(\vec{\psi}_h^k) = \sum_{i=1}^{n} \left\{ \frac{m(V_i)}{\triangle t_k} |\psi_j^k - \psi_j^{k-1} \exp(-\mathrm{i}\Phi_{0j} \triangle t_k)|^2 \right\} + \mathscr{F}^h(\vec{\psi}_h^k). \tag{9}$$

It is generally known that for the case of zero applied current (or voltage), that is, the case with $\Phi_0 = 0$, the above variational principle holds for the standard backward Euler scheme [14]. The establishment of the variational principle for the case with an applied current has not been given before in the literature. It is thus a novel approach to reformulate the original discrete scheme in the more general situation as a variational problem at each time step. Moreover, for $\triangle t_k$ sufficiently small, one can verify that the only critical point of $\mathscr{K}^h$ is the global minimizer of the functional which can be computed by algorithms such as the *Nonlinear Conjugate Gradient* (NCG) method [33]. *Newton's* method and other descent methods may also be used. For the steady state model, the discrete solution automatically satisfies the maximum principle on the SCVT mesh, that is, $|\psi_j| \leqslant 1$ for all j. Moreover, it has been shown that as the mesh refines, the numerical solutions generate function sequences that converge to a minimizer of the continuous energy functional $\mathscr{F}$ [22]. A similar analysis can be done for the time dependent case as well.

For the zero electric potential case, that is $\Phi_0 = 0$, the underlying system is a dissipative gradient flow and the time dependent solution approaches to the steady state as $t \to \infty$. To compute such a steady state of ψ accurately and efficiently, a uniform step size is not appropriate. We employ the following procedure to control the step size $\triangle t_k$:

- Choose an initial time step $\triangle t_1$ and two integers $N_s > N_l > 0$.
- At the kth time step, let N_k be the number of iterations the NCG (or the Newton's method) used. Set $\triangle t_{k+1} = 2\triangle t_k$ if $N_k < N_s$, $\triangle t_{k+1} = \triangle t_k/2$ if $N_k > N_l$; otherwise, $\triangle t_{k+1} = \triangle t_k$.

Of course, for more general cases with $\nabla \Phi_0 \neq 0$ (non-zero applied current), the transient solution behavior can be very important. The time step control must also ensure the accuracy of the time integration.

3.2. Evaluation of physical variables

The physical variables of interest include the free energy, the density of the superconducting Cooper-pairs, the induced magnetic field and the super-current. As the numerical evaluations can be done at any time step, to simplify the presentation, we drop the superscripts that correspond to the time steps.

Once a discrete solution $\{\psi_j\}$ is computed, we can readily obtain the scalar field $\{|\psi_j|^2\}$ which describes the density of superconducting electrons (Cooper-pairs).

As for the super-current given by

$$\mathbf{J}_s = \Im\{\psi^* \nabla_s \psi\} - \mathbf{A}_{0s} |\psi|^2 = -\Re\{(\psi^*(\mathrm{i}\nabla_s \psi + \mathbf{A}_{0s}\psi)\}, \quad \text{on } \mathbb{S}^2 \tag{10}$$

an accurate and gauge invariant scheme has been proposed in [22]. The construction is given as follows. Let $V_{\mathbf{x}_j} = \cup_{x_j \in \tau i j_1 j_2} \tau_{j j_1 j_2}$ be the surface patch containing $\mathbf{x}_j$ with $\tau_{j j_1 j_2}$ denoting the spherical triangle formed by $\mathbf{x}_j$, $\mathbf{x}_{j_1}$ and $\mathbf{x}_{j_2}$. First, project $V_{\mathbf{x}_j}$ onto the tangential plane $S_{\mathbf{x}_j}$ of $\mathbb{S}^2$ at $\mathbf{x}_j$, let $\vec{\mathbf{e}}_{1,\mathbf{x}_j}, \vec{\mathbf{e}}_{2,\mathbf{x}_j}$ be an orthonormal basis of $S_{\mathbf{x}_j}$, and map $S_{\mathbf{x}_j}$ to the (x,y)-plane by an affine map that also maps $\vec{\mathbf{n}}_{\mathbf{x}_j}$ to the z-axis and $\vec{\mathbf{e}}_{1,\mathbf{x}_j}$ to the x-axis (see Fig. 2 for an illustration). Then, define a map $H_{\mathbf{x}_j} : V_{\mathbf{x}_j} \to \mathbb{R}^2$ by the above procedure such that $V'_{\mathbf{x}j} = H_{\mathbf{x}_j}(V_{\mathbf{x}_j})$, on each planar triangle $\triangle \mathbf{x}'_j \mathbf{x}'_{j1} \mathbf{x}'_{j2} = H_{\mathbf{x}_j}(\tau_{j j_1 j_2})$, a linear function $\bar{\psi}_{j j_1 j_2}$ may be uniquely determined by setting $\bar{\psi}_{j j_1 j_2}(\mathbf{x}'_l) = \psi_h(\mathbf{x}_l) = \psi_l$ for $l = j, j_1, j_2$. Next, take

$$v_{j j_k} = \mathrm{i}\frac{\psi_{j_k} \exp(-\mathrm{i}c_{j j_k}) - \psi_j}{\|\mathbf{x}_j - \mathbf{x}_{j_k}\|}, \quad k = 1, 2,$$

as gauge invariant approximations to the components of $\mathrm{i}\nabla_s \psi + \mathbf{A}_{0s}\psi$ along the $\mathbf{x}'_j \mathbf{x}'_{j1}$ and $\mathbf{x}'_j \mathbf{x}'_{j2}$ directions. Finally, for $m = 1, 2$, let $\mathbf{x}'_{jm} = (x_m, y_m), s_{1m} = (-1)^{3-m} y_{3-m} Q, s_{2m} = (-1)^m x_{3-m} Q$ with $Q = \sqrt{x_m^2 + y_m^2}/(x_1 y_2 - x_2 y_1)$ and set $(D^1_{j j_1 j_2}, D^2_{j j_1 j_2})^{\mathrm{T}} = (s_{ml})_{2\times 2}(v_{j j_1}, v_{j j_2})^{\mathrm{T}}$, then $\mathrm{i}\nabla_s \psi + \mathbf{A}_{0s}\psi$ can be approximated at $\mathbf{x}_j$ by

$$(\mathrm{i}\nabla_s \psi + \mathbf{A}_{0s}\psi)(\mathbf{x}_j) \approx \alpha_j = \frac{1}{q} \sum_{\tau_{j j_1 j_2} \subset V_{\mathbf{x}_j}} \left(D^1_{j j_1 j_2} \vec{\mathbf{e}}_{1,\mathbf{x}_j} + D^2_{j j_1 j_2} \vec{\mathbf{e}}_{2,\mathbf{x}_j} \right), \tag{11}$$

where $q = \mathrm{Card}(\{\tau_{j j_1 j_2} \mid \tau_{j j_1 j_2} \subset V_{\mathbf{x}_j}\})$. The discrete super-current is then computed by $\mathbf{J}_s(\mathbf{x}_j) \approx -\Re\{\psi(\mathbf{x}_j)\alpha_j\}$.

This estimate leads to a super-convergent computation of $\mathrm{i}\nabla_s \psi + \mathbf{A}_{0s}\psi$ (thus the super-current) while preserving the discrete gauge invariance.

To find the effect of the spherical geometry on the induced magnetic field, we need to go beyond the leading order term $\mathbf{H}_0$, since the effect only starts to appear in the next order correction [4] which requires the solution of the Maxwell equations:

$$\mathrm{div}\,\mathbf{H}_1 = 0, \quad \mathrm{curl}\,\mathbf{H}_1 = 0, \quad \text{in } \mathbb{R}^3,$$

with interface condition

$$[\mathbf{H}_1 \times \mathbf{n}]_s = \mathbf{J}_s \times \mathbf{n}, \quad \text{on } \mathbb{S}^2,$$

where $\mathbf{n}$ is the unit outer normal to the sphere and $[\cdot]_s$ denotes the jump across the sphere, and $\mathbf{H}_1 \to 0$ at infinity. The total corrected field is given by $\mathbf{H} = H(0,0,1) + \delta \mathbf{H}_1$ where δ represents the thickness of the shell.

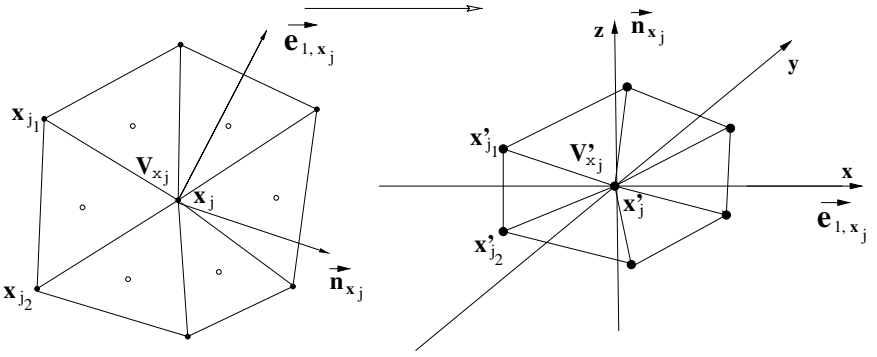

Fig. 2. The mapping $H_{\mathbf{x}_j}$.

As given in [22], to compute $\mathbf{H}_1$, an integral reformulation

$$\mathbf{H}_1(\mathbf{y}) = \int_{S^2} \nabla \frac{1}{\|\mathbf{y}-\mathbf{x}\|} \times \mathbf{J}_s(\mathbf{x}) \mathrm{d}S_{\mathbf{x}}, \quad \forall \mathbf{y} \in \mathbb{R}^3$$

may be used. For any $y \in \mathbb{R}^3 - \mathbb{S}^2$, let $\mathbf{x}_{j_y} \in \{\mathbf{x}_j\}_{j=1}^n$ be the closest generator to $\mathbf{y}$ on the sphere. We then have

$$\mathbf{H}_1(\mathbf{y}) \approx \overline{\mathbf{H}}_1(\mathbf{y}) = \mathbf{G}(\mathbf{y}) \times \mathbf{J}_s(\mathbf{x}_{\mathbf{j}_y}) + \sum_{\mathbf{j} \neq \mathbf{j}_y} \mathbf{m}(\mathbf{V}_\mathbf{j}) \left(\nabla \left(\frac{\mathbf{1}}{\|\mathbf{y}-\mathbf{x}\|} \right) (\mathbf{x}_\mathbf{j}) \times \left(\mathbf{J}_s(\mathbf{x}_\mathbf{j}) - \mathbf{J}_s(\mathbf{x}_{\mathbf{j}_y}) \right) \right), \tag{12}$$

where

$$\mathbf{G}(\mathbf{y}) = \int_{S^2} \nabla \frac{1}{\|\mathbf{y}-\mathbf{x}\|} \mathrm{d}S_{\mathbf{x}} = \begin{cases} 0, & \|\mathbf{y}\| < r, \\ -4\pi r^2 \mathbf{y}/\|\mathbf{y}\|^3, & \|\mathbf{y}\| > r. \end{cases} \tag{13}$$

For $y \in \mathbb{S}^2$, $\mathbf{G}$ may be replaced by its interior and exterior limits to get the corresponding limits of $\mathbf{H}_1(\mathbf{y})$ across the sphere surface. Putting together, a high quality quadrature rule on the sphere is obtained for recovering the field correction.

4. Numerical experiments

We now present the results of our numerical simulations which are performed, without loss of generality, on the unit sphere ($r = 1$).

4.1. The spherical centroidal Voronoi tessellation grid

The SCVT-based grids corresponding to be a constant function $\rho(\mathbf{x}) = 1$ are used in the simulations. For an illustration, see Fig. 3.

More examples of the SCVT grids associated with both a constant density function and non-uniform density functions can be found in [18]. To measure the uniformity of the triangulation on the sphere, we use the following *mesh norm h*:

$$h = \max_{i=1,\ldots,n} h_i, \quad \text{where } h_i = \max_{\mathbf{y} \in V_i} d(\mathbf{x}_i, \mathbf{y}).$$

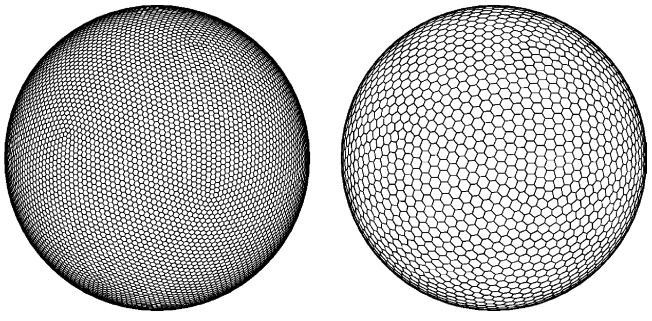

Fig. 3. SCVT meshes with constant density function. Left: $n = 2562$; right: $n = 10{,}242$.

One may see that h_i gives the maximum geodesic distance between the particular generator $\mathbf{x}_i$ and any point in its associated cell V_i and h gives the maximum geodesic distance between any generator and any point in its associated cell. In Table 1, the values of the mesh norm h are listed for different numbers of generators n. For a SCVT with large n, h is very close to the ideal value of $2.2/\sqrt{n}$ for congruent regular hexagons.

4.2. Energy diagrams and solution branches

Similar to thin films, a superconducting thin spherical shell displays the behavior of a type-II superconductor when placed in an applied magnetic field. Below the critical transition temperature, as the magnitude of applied magnetic field increases, vortices start to appear in the spherical shell.

To describe the equilibrium vortex state, numerical experiments are conducted to probe the landscape of the reduced free energy functional corresponding to various values of the applied magnetic field. Some preliminary experiments have been made in [22]. Here, more extensive simulation results are reported.

We first set $\epsilon = 0.2$ and vary the value of the applied field for the steady state G–L equation. When the magnetic field is absent ($H = 0.0$), the energy minimizer of $\mathscr{F}$ is given by the pure superconducting solution $\psi = \exp(\mathrm{i}\theta)$ for any constant angle θ. In our simulation, with the initial iteration given by $\psi(\mathbf{x}) = 0.5\exp(\mathrm{i}\frac{\pi}{4})$ everywhere, a pure superconducting solution $\psi = \exp(\mathrm{i}\frac{\pi}{4})$ is found numerically. As H becomes larger, we expect that the solution ψ starts to contain vortices, that is, $\psi(\mathbf{x}) = 0$ for some points $x \in \mathbb{S}^2$. Due to the domain symmetry, the vortices will appear in pairs (vortex and anti-vortex, if observed from the center of the sphere, or simply pairs of vortices of the same orientation if all observed from the positive z-direction). This is an interesting effect that can be observed in a spherical geometry but not for simple planar geometry. A consequence of this symmetry is that, to present the various vortex structures, most of the figures are given by the density plots of $|\psi|$ in the northern (upper) hemisphere. The plots on the southern hemisphere can be produced through a simple mirror reflection.

As H increases, more vortices appear (again in pairs). We use the path-following approach to probe the energy landscape. To ensure that we may find different vortex solutions, due to the energy barrier [9], sometimes we intensionally *plant* some vortices in our initial iteration.

A solution branch is usually found by path-following with respect to the parameter H. Jumps to other branches occur at some values of H, then new branches are probed. Repeating such processes, various solution branches are found numerically and the results are given in Fig. 4. The switches between different branches are also depicted in Fig. 5 where the arrow lines indicate that jumps between the particular vortex configurations take place in the numerical simulation.

In Fig. 6, the density plots of $|\psi|$ illustrate the basic vortex structures corresponding to the solution branches. The color scheme used in all density plots given in this paper, unless otherwise depicted in the legend, takes dark rose-wood red for $|\psi| = 1$ and gradually changes into green for $|\psi| = 0.5$ then to blue for $|\psi| = 0.0$. For monochrome prints, vortices can be identified through isolated higher intensity regions. In Fig. 7, the corresponding super-current $\mathbf{J}_s$ is depicted for the solution with 6 pairs of vortices (a) given in Fig. 6.

The plot of the discrete global minimum energy $\mathscr{F}^h$ versus the magnetic field strength H is shown in Fig. 8, together with the plot of a smoothly fitted polynomial done is MATLAB. Note that the global minimum energy curve of $\mathscr{F}^h$ is in fact given by the lower envelope of the family of energy curves corresponding to

Table 1
Number of generators vs. mesh norms

n	12	42	162	642	2562	10242	40962
h	0.6524	0.3609	0.1793	0.0892	0.0456	0.0238	0.0119

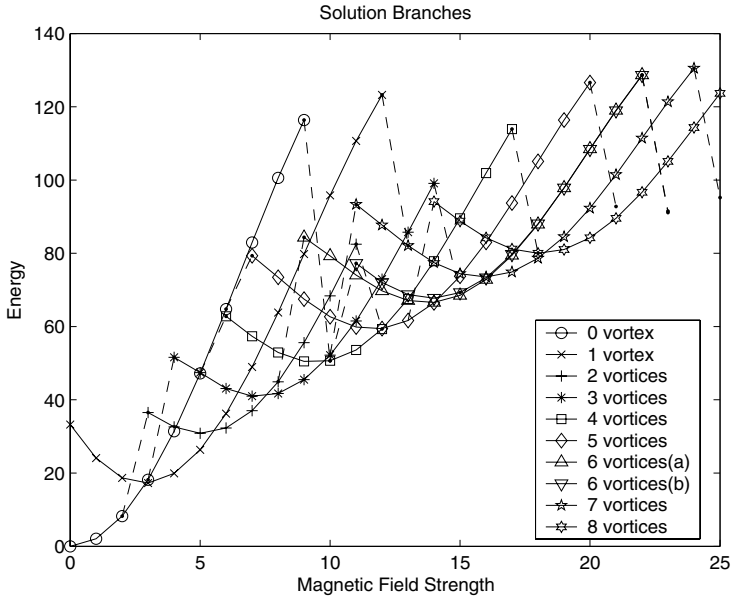

Fig. 4. Solution branches for $\epsilon = 0.2$.

different solution branches in Fig. 4. We compute the derivative of the fitted polynomial to give a plot of this magnetization curve, that is, a plot of the derivative of the global minimum energy against the applied magnetic field. Note that such a curve is different from the ones generated by differentiating along an individual solution branch (see for instance those presented in [9]). The numerical values of the discrete minimum energy are given in Table 2.

A couple of interesting observations can be made based on the above numerical computations. First of all, the solution of the single vortex pair persists when the applied magnetic field decreases. Even for $H = 0$, such a vortex solution still exists, though it is no longer the global energy minimum at small H.

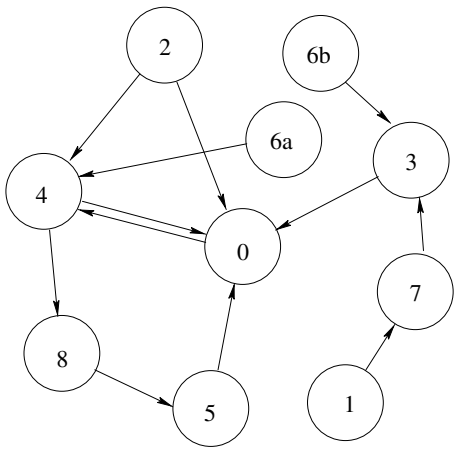

Fig. 5. The switches between solution branches for $\epsilon = 0.2$.

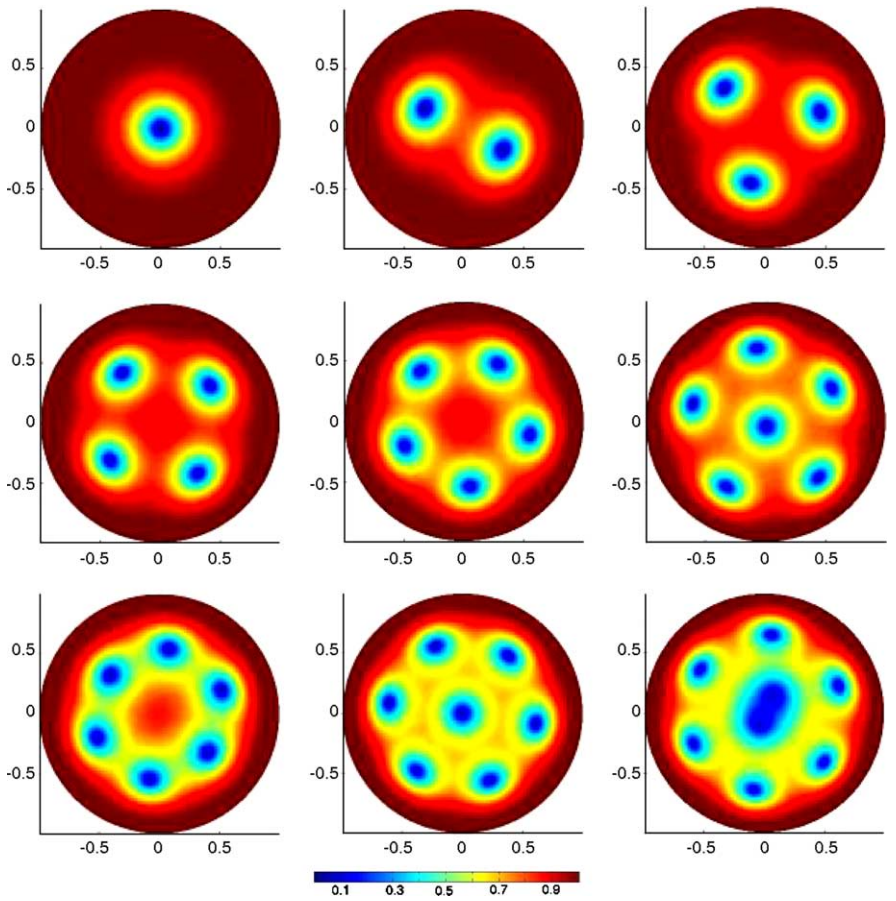

Fig. 6. Vortex configurations (density plots of $|\psi|$) corresponding to the values of H and $\mathscr{F}^h$ (given in parenthesis): Top row (from left to right): 1 pair of vortices ($H=4.0$, $\mathscr{F}^h = 19.973$), 2 pairs of vortices (7.0, 37.027), 3 pairs of vortices (9.0, 45.490); second row (from left to right): 4 pairs of vortex (11.0, 53.608), 5 pairs of vortices (13.0, 61.636), 6 pairs of vortices (a) (15.0, 68.511); third row (from left to right): 6 pairs of vortices (b) (16.0, 73.331), 7 pairs of vortices (18.0, 78.633), 8 pairs of vortices (20.0, 84.234); Bottom: legend.

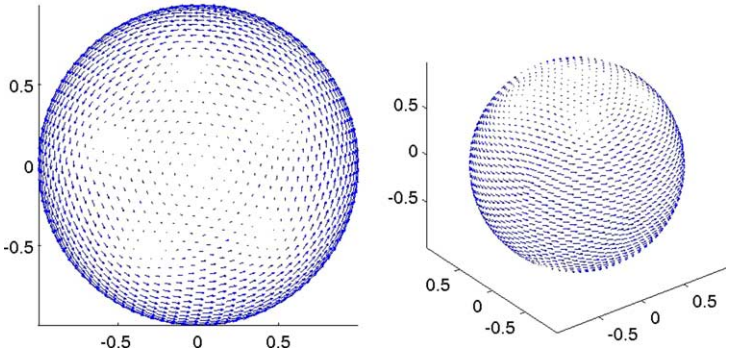

Fig. 7. Super-current $\mathbf{J}_s$ for the solution with 6 pairs of vortices (a) and $H=15.0$, $\mathscr{F}^h = 68.511$. Left: top view; right: 3-D view.

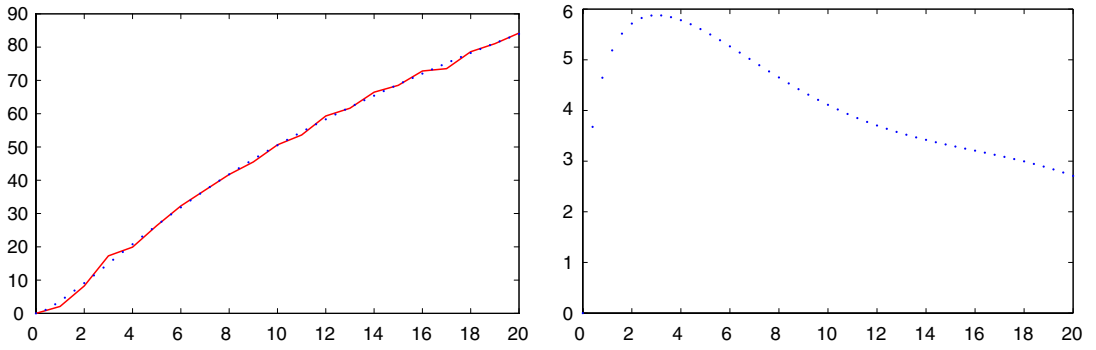

Fig. 8. Minimum energy $\mathscr{F}^h$ with its polynomial fitting and the magnetization curve.

Secondly, there are two different patterns corresponding to 6 pairs of vortices with very similar energy values, though the one with one pair at the center always carries a slightly smaller energy value. Such an observation is similar to the case of the vortex pattern simulated using the original G–L equations in two dimensions [12,35,36].

4.3. The effect of thickness

To see the effect of thickness of the sphere shell, we set the parameter $\delta = 0.1$ and $\delta = 0.2$ respectively and compute the corrected magnetic field corresponding to Fig. 7 based on the discussion given in Section 3.2. Three dimensional vector plots and the plots in a vertical cross-section are given in Fig. 9. From the figures, we can observe that the induced fields tilt more for thicker spheres.

4.4. Changes in the coherence length

In order to see the effect of coherence length ϵ, we reset it to be 0.05. As the vortex size is expected to be smaller, a finer SCVT mesh with $n = 40{,}962$ is used to ensure that the vortex shape can be accurately resolved.

First, we take $H = 25.0$ and compute a couple of different solution branches with 10 pairs of vortices, see Fig. 10. Clearly, the vortex size is indeed smaller than that of $\epsilon = 0.2$. The 10 pairs of vortices solution with 3 pairs at the center has the smallest energy value.

Then, we consider $H = 50.0$. Four different vortex configurations are found with 19, 20, 21 and 22 pairs of vortices respectively, see Fig. 11. The energy value decreases when the vortex number increases. The corresponding super-current $\mathbf{J}_s$ of the solution of 20 pairs of vortices is shown in Fig. 12. Though having little physical significance, the plots of the real and imaginary parts of the order parameter of the solution of 22

Table 2
Minimum energy $\mathscr{F}^h$ vs. magnetics field strength H

H	0.0	1.0	2.0	3.0	4.0	5.0	6.0
$\mathscr{F}^h$	0.0000	2.0863	8.2457	17.2853	19.9073	26.3519	32.2881
H	7.0	8.0	9.0	10.0	11.0	12.0	13.0
$\mathscr{F}^h$	37.0270	41.7372	45.4901	50.6589	53.6079	59.3215	61.6361
H	14.0	15.0	16.0	17.0	18.0	19.0	20.0
$\mathscr{F}^h$	66.4742	68.5107	72.8404	73.5258	78.6327	81.0200	84.2344

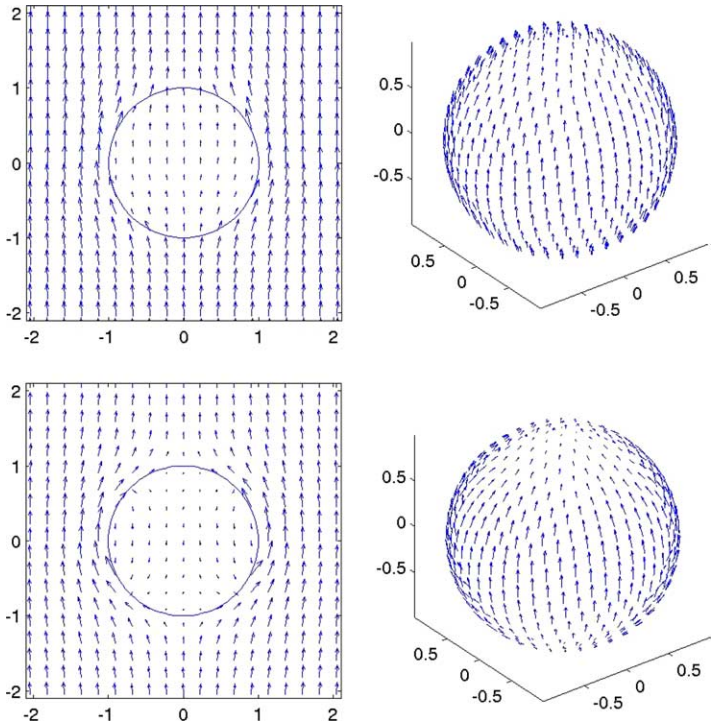

Fig. 9. Corrected magnetic field **H**. Top: $\delta = 0.1$; bottom: $\delta = 0.2$; left: on the plane $y = 0$; right: on the surface $\{\mathbf{x} | \|\mathbf{x}\| = 1.1\}$.

pairs of vortices are given in Fig. 13 to demonstrate the complexity in the numerical solution that contains a large number of vortices and the interesting fact that more variations are displayed near the equator despite of the lack of vortices in such a region.

Finally, we show a vortex configuration with 144 pairs of vortices which is obtained by setting $\epsilon = 0.03$ and $H = 300.0$, see Fig. 14. As H gets sufficiently large, the hexagonal vortex patterns become more visible and dominant. However, topological considerations preclude the appearance of a perfect hexagonal lattice on the sphere. Thus, the existence of defects in the lattices is a generic fact associated with the spherical geometry. For similar discussions, we refer to [11].

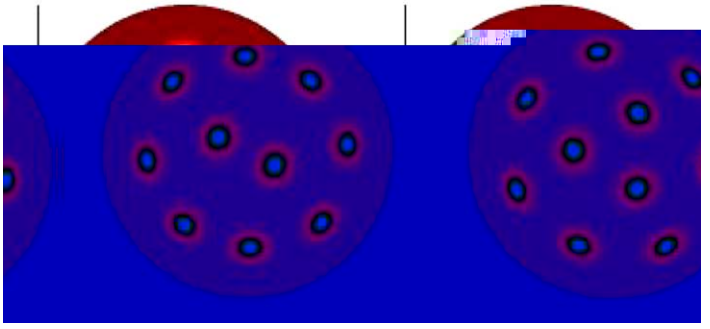

Fig. 10. Configurations for 10 vortex pairs, $H = 25$, $\mathscr{F}^h = 225.284$ (left) and 223.026 (right).

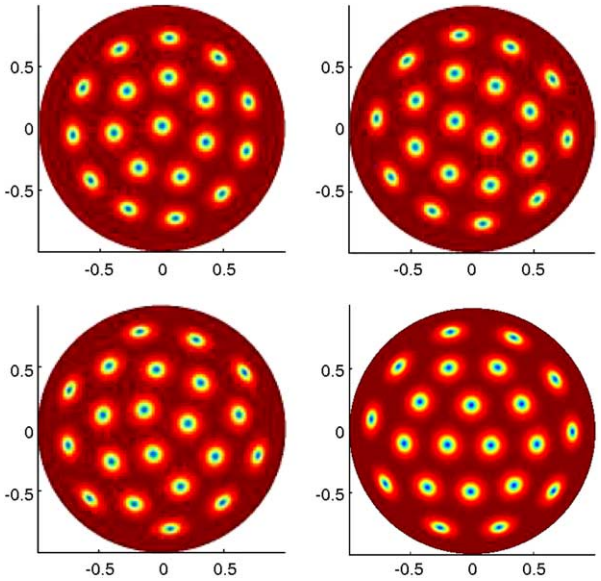

Fig. 11. Vortex configurations for $H=50.0$. Top row (from left to right): 19 pairs of vortices ($\mathscr{F}^h = 439.283$), 20 pairs of vortices ($\mathscr{F}^h = 414.834$), bottom row (from left to right): 21 pairs of vortices ($\mathscr{F}^h = 403.073$), 22 pairs of vortices ($\mathscr{F}^h = 399.791$).

4.5. Vortex nucleation

To examine the vortex nucleation process, the time dependent equations need to be solved. As an example, we set $H=22$ and $\Phi_0=0$ and solve the time dependent equation with an initial superconducting state described by $\psi(\mathbf{x}) = \exp(\mathrm{i}\frac{7\pi}{20})$. We use $\triangle t_1=0.002$ and compute the time dependent solutions on a SCVT grid with $n=10{,}242$. A variable time step control strategy is used with $N_s=6$ and $N_l=10$. The simulation takes a total 31 iterations to reach a steady state. In Fig. 15, the evolution of vortex configurations in time is illustrated and the corresponding values of the energy $\mathscr{F}^h$ are also given. We note that special legends are provided in Fig. 15 as the color schemes vary in time. It can be observed that the vortex pairs nucleate near the equators and then they split and move towards the poles and interact with other existing vortices until an equilibrium configuration is stabilized. Such a simulation gives a more clear demonstration of the vortex

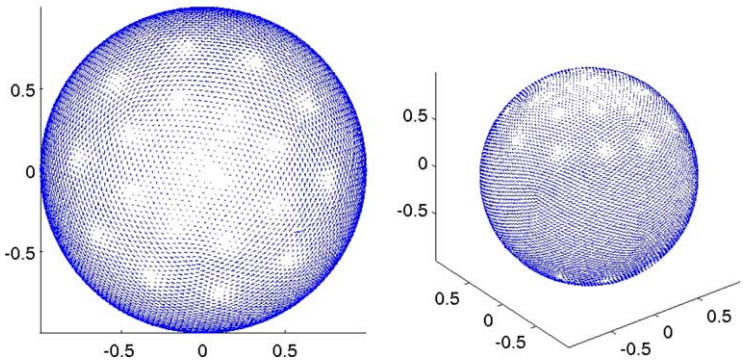

Fig. 12. Super-current $\mathbf{J}_s$ for the solution with 20 pairs of vortices, $H=50.0$, $\mathscr{F}^h = 414.834$. Left: top view; right: 3-D view.

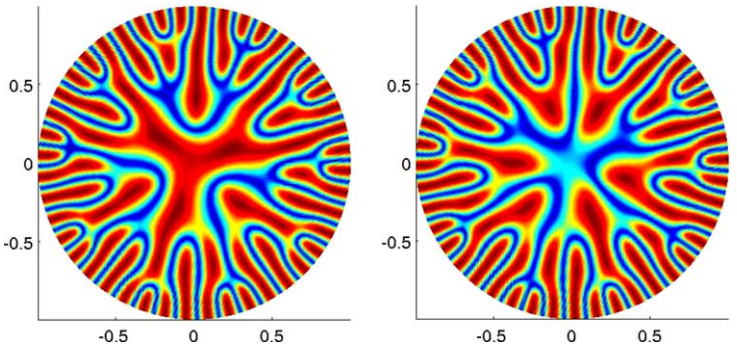

Fig. 13. The absolute value of the real (left) and imaginary (right) parts of ψ corresponding to the solution with 22 vortices for $H = 50.0$ with $\mathscr{F}^h = 399.791$.

nucleation process than the ones computed on a planar geometry (see for example, [2,20]), as the *ghost vortices* are not computationally visible in the exterior of the planar sample.

4.6. Vortex motion

With a prescribed applied voltage (or current), vortices move due to the Lorenz force. To simulate the vortex motion, the prescribed electric potential is set to be $\Phi_0(x,y,z) = cx$ for various values of c which represents the strength of the applied current. The time dependent equation with such a given potential is solved with a constant time step $\triangle t$. For $c > 0$, this prescribed scalar potential models an applied voltage change from the negative x direction to the positive x direction which creates a gradient in the effective magnetic field and leads to the Lorenz force. The use of a prescribed Φ_0 in the simplified time dependent G–L model to represent the effect of the applied voltage has been justified in suitable parameter regimes [16], which also implies that the screening effect of the supercurrent on the total electric field is ignored in the present context [40]. Nevertheless, we expect much of the findings would remain true when the full set of original G–L equations is solved (see the related demonstrations in [16]).

In the next set of simulations, we first let $c = 5.0$, $\epsilon = 0.2$, $H = 15.0$, $\triangle t = 0.025$, and take the SCVT grid with $n = 10{,}242$. An initial state is given by the 6 pairs of vortices with one pair at the center computed

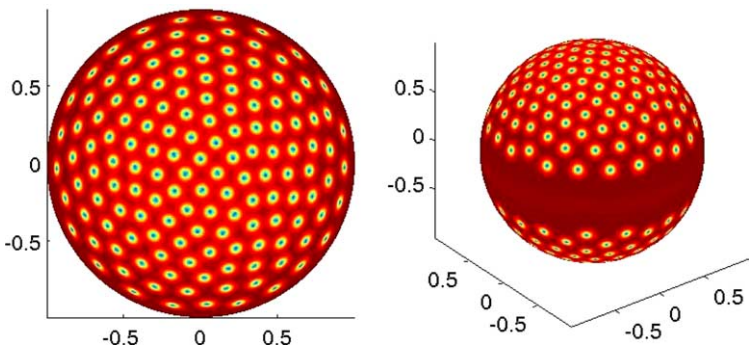

Fig. 14. Vortex configurations with 144 pairs of vortices ($H = 300.0$, $\mathscr{F}^h = 2077.534$) and the formation of a hexagonal lattice with defects. Left: top view; right: 3-D view.

earlier. The motion paths of each individual vortex are shown in Fig. 16 at several time instances from $t=0$ to

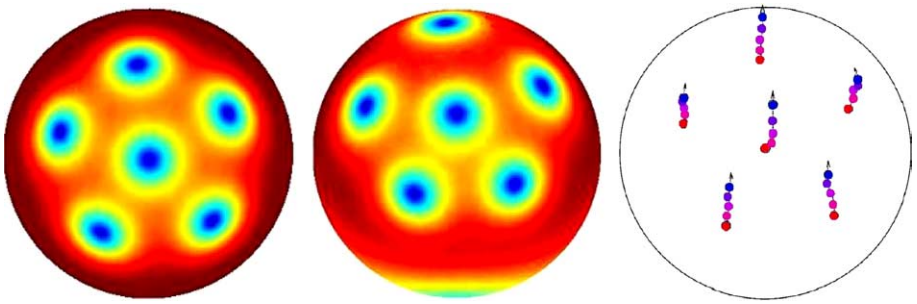

Fig. 16. The motion of vortices with $H=15.0$ and $\Phi_0(x,y,z)=5.0x$. Left: initial state at $t=0$, $\mathscr{F}^h = 68.511$; center: solution at $t=1.0$, $\mathscr{F}^h = 92.642$; right: the path of vortex motion from $t=0$ to $t=1.0$.

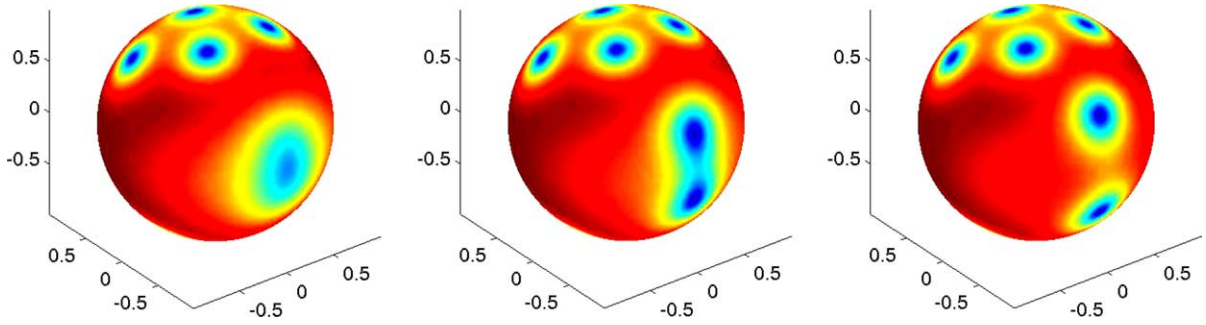

Fig. 17. The nucleation and the splitting of vortex pairs near equator. From left to right: ($t=1.0$, $\mathscr{F}^h = 92.642$), (1.15, 93.158), (1.2, 89.827).

coherence length is given by $\epsilon=0.05$ and the applied magnetic field is $H=50.0$. An initial state given by a solution with 22 pairs of vortices is adopted.

Although the existence of a steady state is still possible for very small c which corresponds to the existence of the *critical current* as discussed in [13], for $c=2.5$, the motion of the vortex structure becomes evident, see Fig. 18 for the energy variation in time. Physically speaking, this means that the applied current is inserting a Lorenz force that is strong enough to push the vortices overcome the energy barrier formed by the applied magnetic field near the equator of the sphere. The evolution seems to be following a quasi-periodic orbit, but the period cannot be exactly predicted based on the simulation.

For larger c, the periodic motion becomes more transparent. We enlarge c to $c=5.0$, $c=7.5$, $c=10.0$ and $c=15.0$, and repeat the above computation again. The almost time periodic motion of the vortex structure not only appears but also persists as demonstrated by the energy plots in Fig. 19 which includes plots of the free energy $\mathscr{F}^h$ for $c=5.0$, 7.5, 10.0 and 15.0. Based on the energy curve, we see that the approximate time periods are about 5.6, 1.6, 0.8 and 1.2 for $c=5.0$, 7.5, 10.0, 15.0, respectively. The vortex configurations at some particular instances in time are presented in Fig. 20 for $c=10.0$ and $c=15.0$. The energy oscillation is demonstrated in Figs. 18 and 19.

When c is taking an even larger value, say for $\Phi_0=25.0x$, the vortex structure starts to collapse as time goes by, and the solution eventually turns into a normal or near normal state. Thus, we have observed the transition of the solution of the time-dependent G–L equation with an applied current/voltage

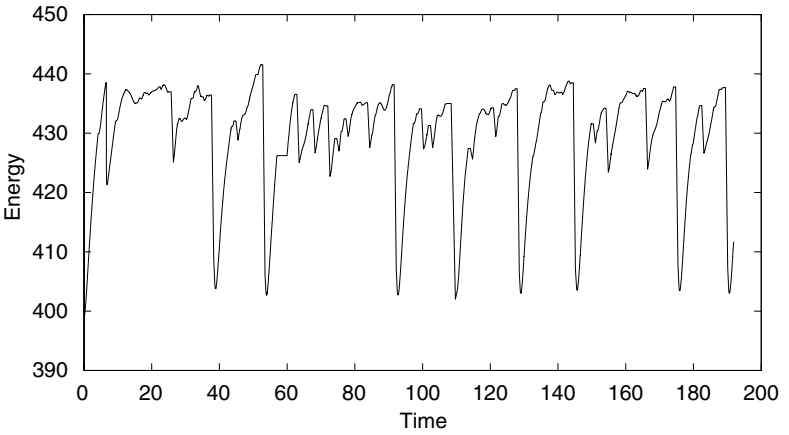

Fig. 18. The energy evolution in time with $H=50.0$ and applied voltage $\Phi_0(x,y,z)=2.5x$ starting from the configuration with 22 vortices.

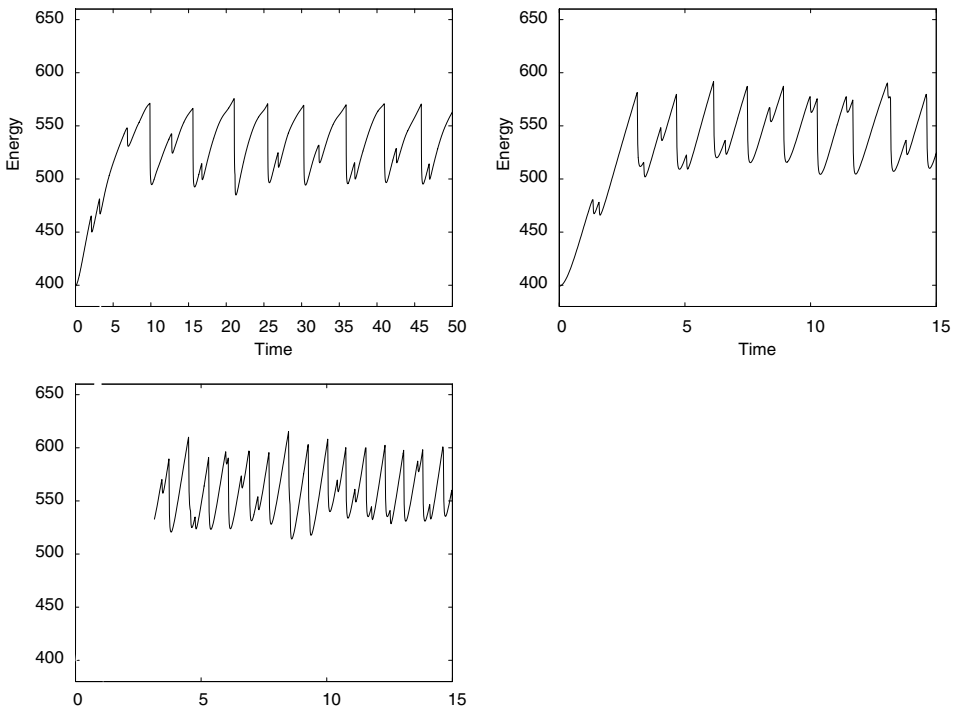

from the existence of an equilibrium vortex structure to a near time-periodic persistent motion, to a near normal state. Such simulations have not been reported much in the literature [13]. Naturally, more detailed studies on dependence of the period on the parameter c as well as the I–V characteristics would require more extensive computation and they are left for future investigations.

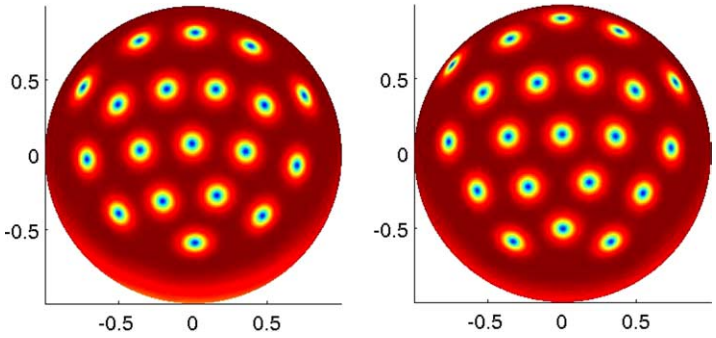

Fig. 20. Vortex configuration with applied voltage. Left: $c=10.0$, $t=2.7$, $\mathscr{F}^h = 559.16$, 19 pairs of vortices; right: $c=15.0$, $t=2.0$, $\mathscr{F}^h = 529.68$, 21 pairs of vortices.

5. Conclusions

In this paper, the numerical approximation of the G–L model for a superconducting hollow sphere is studied. It enjoys the discrete gauge invariance and is based on the recently developed SCVT. It utilizes the properties of the SCVT and the discrete gauge invariance to accurately compute the various solution branches, vortex nucleation patterns and vortex dynamics on the sphere. It also allows us to make some physically interesting observations on the vortex configurations and dynamics. With the use of actual experimental data, these investigations may lead to more meaningful comparisons with some of the current experimental studies in superconductivity.

The simulation results presented here clearly demonstrate the effectiveness of the SCVT based numerical discretization methods even for nonlinear problems, especially when the physical and mathematical structures of the problem can be utilized. It is expected that the SCVT will also find other applications related to the computation of physical models on spheres, for instance, in the simulation of shallow water models and global circulation models. Meanwhile, the concept of centroidal Voronoi tessellations has also been developed for general constrained surfaces [17]. Thus, in the context of superconductivity, we also look forward to the applications of these optimal tessellations in the more general setting for simulating the properties of thin superconductors having other geometric structures [32].

Acknowledgement

We would like to thank the referees for providing their valuable comments and additional references.

References

[1] A. Aftalion, Q. Du, The bifurcation diagram for the Ginzburg–Landau system for superconductivity, Physica D 163 (2001) 94–105.
[2] B. Baelus, F. Peeters, Dependence of the vortex configuration on the geometry of mezoscopic flat samples, Phys. Rev. B 65 (2002) 104515.
[3] B. Baelus, F. Peeters, V. Schweigert, Saddle-point states and energy barriers for vortex entrance and exit in superconducting disks and rings, Phys. Rev. B 63 (2001) 144517.
[4] S. Chapman, Q. Du, M. Gunzburger, A variable thickness thin film model for superconductivity, ZAMP 47 (1995) 410–431.
[5] S. Chapman, Q. Du, and M. Gunzburger, A Ginzburg–Landau model for superconducting shells, preprint, 2004.

[6] S. Chapman, D. Heron, The Motion of superconducting vortices in thin films of varying thickness, SIAM J. Appl. Math. 58 (1998) 1808–1825.
[7] Z. Chen, S. Dai, Adaptive Galerkin method with error control for a dynamical Ginzburg–Landau model in superconductivity, SIAM J. Numer. Anal. 38 (2001) 1961–1985.
[8] M. Coffey, London model for the levitation force between a horizontally oriented point magnetic dipole and superconducting sphere, Phys. Rev. B 65 (2002) 214524.
[9] P. Deo, V. Schweigert, F. Peeters, Hysteresis in mezoscopic superconducting disks: The Bean–Livingston barrier, Phys. Rev. B 59 (1999) 6039.
[10] S. Ding, Q. Du, Critical magnetic field and asymptotic behavior for superconducting thin films, SIAM J. Math. Anal. 34 (2002) 239–256.
[11] M. Dodgson, M.A. Moore, Vortices in a thin-film superconductor with a spherical geometry, Phys. Rev. B 55 (1997) 3816–3831.
[12] R. Donnelly, Quantized Vortices in Helium II, Cambridge University Press, Cambridge, 1991.
[13] Q. Du, Diverse vortex dynamics in superfluids, Contemp. Math., 329 Current trends in Scientific Computing, 105-117, AMS, 2003.
[14] Q. Du, Discrete gauge invariant approximations of a time-dependent Ginzburg–Landau model of superconductivity, Math. Comp. 67 (1998) 965–986.
[15] Q. Du, V. Faber, M. Gunzburger, Centroidal Voronoi tessellations: applications and algorithms, SIAM Rev. 41 (1999) 637–676.
[16] Q. Du, P. Gray, High-kappa limit of the time dependent Ginzburg–Landau model for superconductivity, SIAM J. Appl. Math. 56 (1996) 1060–1093.
[17] Q. Du, M. Gunzburger, L. Ju, Constrained centroidal Voronoi tessellations on general surfaces, SIAM J. Sci. Comput. 24 (2003) 1488–1506.
[18] Q. Du, M. Gunzburger, L. Ju, Voronoi-based finite volume methods, optimal Voronoi meshes, and PDEs on the sphere, Comput. Meth. Appl. Mech. Engrg. 192 (2003) 3933–3957.
[19] Q. Du, M. Gunzburger, J. Peterson, Analysis and approximation of the Ginzburg–Landau model of superconductivity, SIAM Rev. 34 (1992) 54–81.
[20] Q. Du, M. Gunzburger, J. Peterson, Computational simulations of type-II superconductivity including pinning mechanisms, Phys. Rev. B 51 (1995) 16194–16203.
[21] Q. Du, L. Ju, Finite volume methods on spheres and spherical centroidal Voronoi tessellations, IMA preprint, No. 1918, 2003.
[22] Q. Du, L. Ju, Approximations of a Ginzburg–Landau model for superconducting hollow spheres based on spherical centroidal Voronoi tessellations, Math. Comp., in press.
[23] Q. Du, F. Lin, Ginzburg–Landau vortices, dynamics, pinning and hysteresis, SIAM J. Math. Anal. 28 (1999) 1265–1293.
[24] Q. Du, R. Nicolaides, X. Wu, Analysis and convergence of a covolume approximation of the Ginzburg–Landau models of superconductivity, SIAM J. Numer. Anal. 35 (1998) 1049–1072.
[25] W. E, Dynamics of vortices in Ginzburg–Landau theories with applications to superconductivity, Physica D 77 (1994) 383–404.
[26] H. Fink, V. Grunfeld, Temperature dependence of fluxoid quantization in a superconducting hollow cylinder, Phys. Rev. B 22 (1980) 2289.
[27] V. Fomin, V. Misko, J. Devreese, V. Moshchalkov, Superconducting mesoscopic square loop, Phys. Rev. B 58 (1998) 11703–11715.
[28] D. Gropp, H. Kaper, G. Leaf, D. Levine, M. Plumbo, V. Vinokur, Numerical simulation of vortex dynamics in type-II superconductors, J. Comp. Phys. 123 (1996) 254–266.
[29] E. Hebey, Sobolev Spaces on Riemannian Manifolds, Springer, Berlin, 1991.
[30] B. Ianotta, Music of the spheres, New Scientist 31 (1996) 28–31.
[31] H. Jadallah, J. Rubinstein, P. Sternberg, Phase transition curves for mesoscopic superconducting samples, Phys. Rev. Lett. 82 (1999) 2935.
[32] V. Moshchalkov, L. Gielen, C. Strunk, R. Jonckheere, X. Qiu, C. Van Haesendonck, Y. Bruynseraede, Effect of sample topology on the critical fields of mesoscopic superconductors, Nature 373 (1995) 319–321.
[33] E. Polak, Computational Methods in Optimization, Academic Press, New York, 1971.
[34] B. Richter, R. Warburton, A new generation of superconducting gravimeters, in: Proceedings of the 13th International Symposium on Earth Tides, Brussel, Série Géophysique, Royal Observatory of Belgium, 1998, pp. 545–556.
[35] V. Schweigert, F. Peeters, Flux penetration and expulsion in thin superconducting disks, Phys. Rev. Lett. 83 (1999) 2409–2412.
[36] V. Schweigert, F. Peeters, P. Deo, Vortex phase diagram for mesoscopic superconducting disks, Phys. Rev. Lett. 81 (1998) 2783–2786.
[37] R. Tao, X. Zhang, X. Tang, P. Anderson, Formation of high temperature superconducting balls, Phys. Rev. Lett. 83 (1999) 5575–5578.
[38] B. Tent, D. Qu, D. Shi, W. Bresser, P. Boolchand, Z. Cai, Angle dependence of magnetization in a single-domain $YBa_2Cu_3O_x$ sphere, Phys. Rev. B 58 (1998) 11761.
[39] M. Tinkham, Introduction to Superconductivity, second ed., McGraw-Hill, New York, 1994.

[40] D.Y. Vodolazov, F.M. Peeters, Dynamic transitions between metastable states in a superconducting ring, Phys. Rev. B 66 (2002) 054537.
[41] Y. Xiao, S. Buchman, G. Keiser, B. Muhlfelder, J. Turneaure, C. Wu, Magnetic flux distribution on a spherical superconducting shell, Physica B 194–196 (1994) 65–66.
[42] J. Yeo, M. Moore, Non-integer flux quanta for a spherical superconductor, Phys. Rev. B 58 (1998) 10785–10789.